Supplement of Atmos. Chem. Phys., 20, 5697–5727, 2020
https://doi.org/10.5194/acp-20-5697-2020-supplement

Atmospheric Chemistry and Physics
Open Access
EGU

Supplement of

The role of plume-scale processes in long-term impacts of aircraft emissions

Thibaud M. Fritz et al.

Correspondence to: Sebastian D. Eastham (seastham@mit.edu)

Table S1: List of input parameters to APCEMM. For each parameter, an order of magnitude is provided.

Description	Typical value / unit
Temperature	200 - 250 K
Pressure	~ 220 hPa
Flight-level RH	varies
Horizontal diffusion coefficient	~ 20 m^2/s
Vertical diffusion coefficient	0.15 m^2/s
Shear	0 - 8 m/(km.s)
Longitude	-180 - 180
Latitude	-90 - 90
Day of emission	1 - 365
Time of emission	0 - 24
Background mixing ratios	varies
Photolysis rates	varies (from GEOS-Chem)
NO_x emission index	5 - 20 g/kg fuel
CO emission index	~ 1 g/kg fuel
UHC emission index	~ 0.5 g/kg fuel
SO_2 emission index	~ 1 g/kg fuel
S(IV) to S(VI) conversion factor	~ 5%
Black carbon mass emission index	~ 15 mg/kg fuel
Black carbon radius	~ 20 nm
Total fuel flow	~ 1-4 kg fuel/s
Aircraft mass	~ 50 - 100 tonnes
Initial updraft velocity	~ 0 - 10 cm/s
Updraft velocity decay timescale	1 hour
Moist layer depth	~ 500m
Temperature lapse rate	~ -6K/km

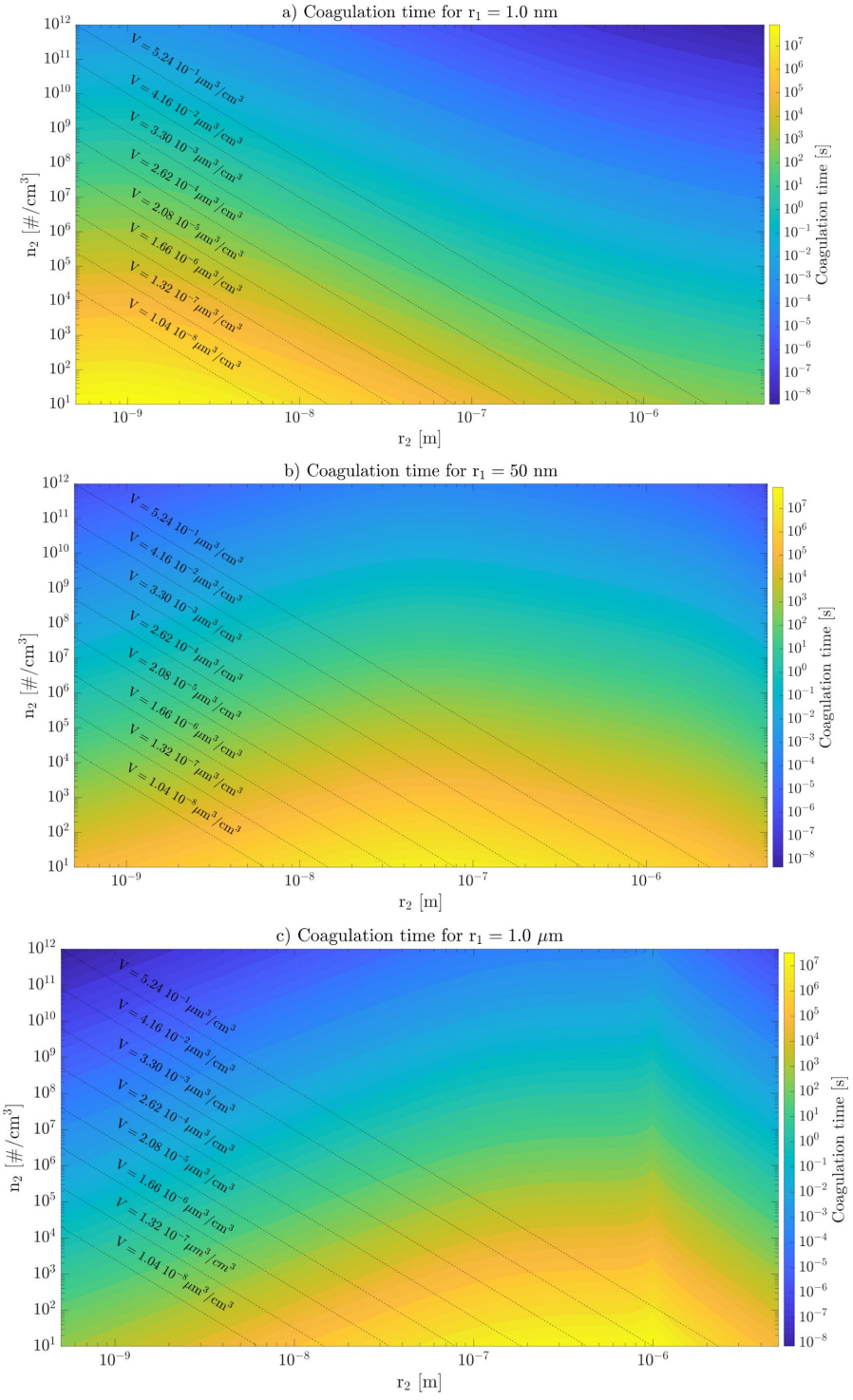

Figure S1: Coagulation timescales for different number densities (n_2) of the scavenging particles with a particle radius (r_2). The scavenged particle has a radius r_1.

Figure S1 shows scavenging timescales as a function of the number densities and radius of the scavenging particles (particle 2) with different radius of the scavenged particle (particle 1). Timescales decrease with increasing difference between r_1 and r_2.

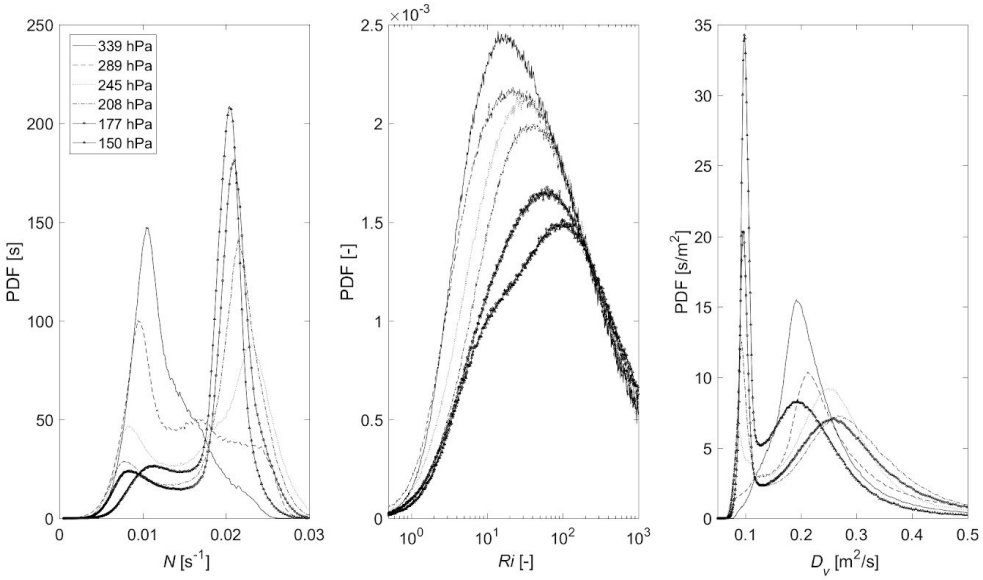

Figure S2: Probability distribution functions of the Brunt-Väisäla frequency, Richardson number, and vertical diffusion coefficient at different pressures obtained from the Modern-Era Retrospective analysis for Research and Applications, Version 2 (MERRA-2) dataset for the year 2015.

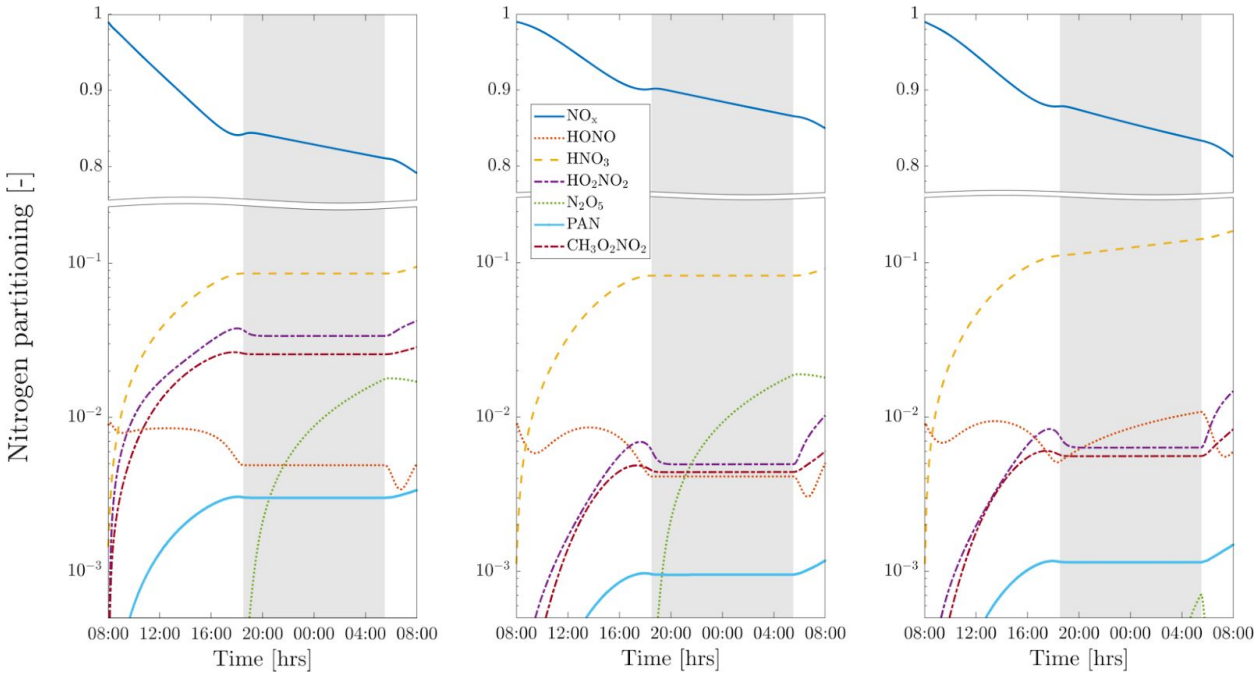

Figure S3: Partitioning of emitted nitrogen species as computed according to the instant dilution approach (left), the plume model in an ice subsaturated environment (middle), and the plume model in an ice supersaturated environment (right). Pressure and temperature are set to 240 hPa and 210 K respectively.

In addition to changes in the NO_x lifetime, we find that the partitioning of nitrogen between different species is significantly different between the instant dilution approach and APCEMM. Figure S3 shows the partitioning of emitted NO_x as a function of time for the two models. Results in an ice supersaturated environment are also displayed as heterogeneous chemistry on contrail ice crystals has a significant on the nitrogen partitioning.

For the ice subsaturated case, HONO and nighttime N_2O_5 match with good precision between the instant dilution and the plume models. However, mixing ratios of NO_x, HO_2NO_2, PAN and $CH_3O_2NO_2$ are lower with APCEMM. The discrepancies do not reduce with time indicating that the instant dilution approach leads to a non-vanishing perturbation in the nitrogen partitioning which affects photochemistry, heterogeneous chemistry and aerosol formation.

The different results between the subsaturated and supersaturated cases are consequences of heterogeneous chemical reactions on the surface of ice crystals, which have a larger aerosol surface area, compared to black carbon or sulfate aerosols.

The differences between both simulations lie in the NO_x, HNO_3, HONO and N_2O_5 mixing ratios, which are direct consequences of the following heterogeneous reactions:

$$2NO_2 + H_2O_{(l,s)} \rightarrow HNO_3 + HONO$$
$$N_2O_5 + H_2O_{(l,s)} \rightarrow 2HNO_3.$$

In an environment with a high relative humidity, heterogeneous chemistry leads to NO_x and HO_x sequestration. The production of HNO_3 through N_2O_5 hydrolysis leads to a larger fraction of HNO_3 as a percentage of NO_y. In the subsaturated (resp. supersaturated) case, the fraction is 15.3% (resp. 25.4%). The instant dilution assumption predicts a HNO_3 fraction of 14.8% in the subsaturated case. The nighttime behavior of HONO is also affected by heterogeneous depletion of NO_2. Halogen reservoir species do not play an important role in the nitrogen partitioning because of their relatively low abundance around the tropopause. Flying higher, in the stratosphere, could change this behavior.

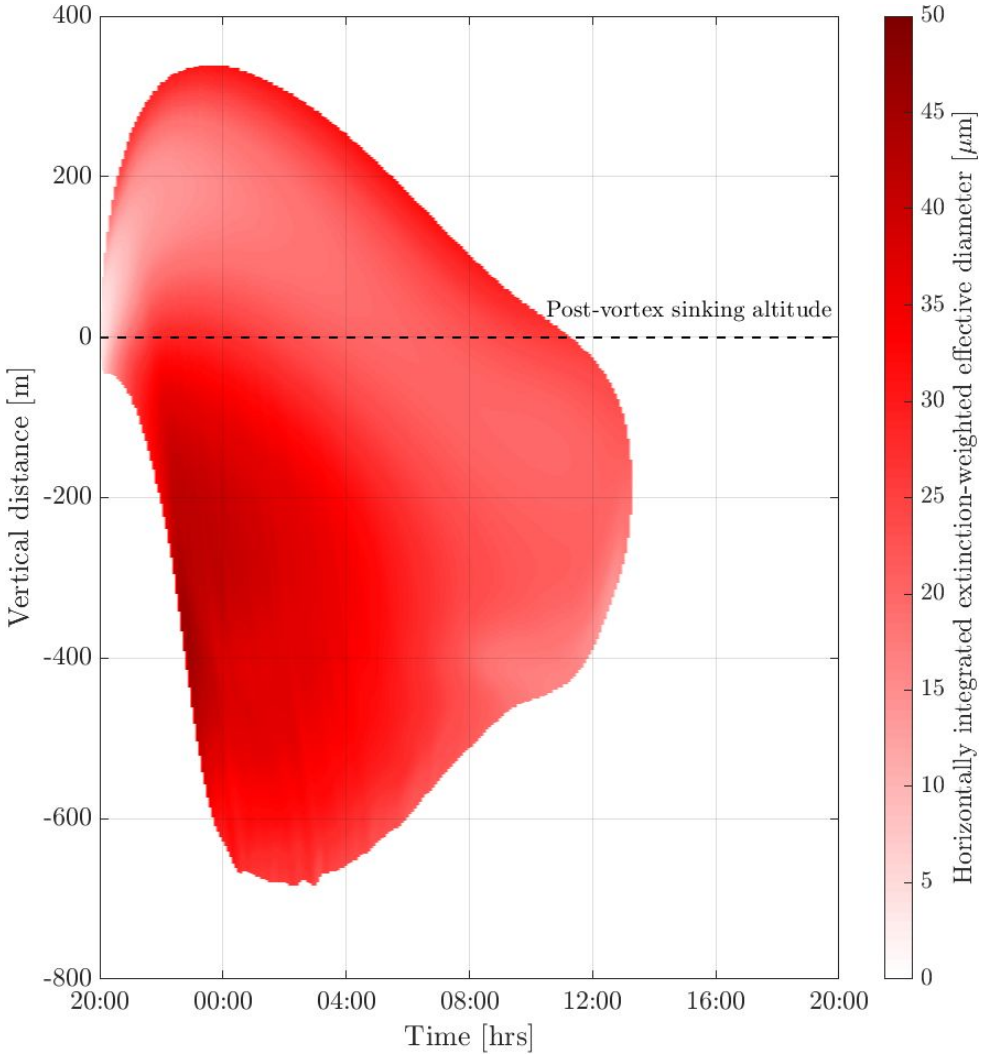

Figure S4: Contrail effective radius, extinction-weighted and horizontally-integrated. Only regions where the mean horizontally-integrated extinction is greater than 10^{-6} are displayed. The vertical axis represents the distance with respect to the flight altitude after vortex sinking. The flight altitude before vortex sinking is at a pressure altitude of 10.6 km. Vortex sinking causes the plume to settle at a new altitude, 112 m lower, corresponding to the origin of the vertical axis. An upward velocity of 5 cm s^{-1}, a relative humidity of 108.0% and a temperature of 210 K are chosen.

Figure S4 shows the contrail effective radius, weighted by extinction, integrated horizontally. Contrails consist of a core region where the relative humidity is close to 100% (because the mixing of supersaturated air happens on a timescale much greater than the timescale required for the ice crystals to grow) and an outer region, forming a fall-streak. Both of these regions have different microphysical properties. The core consists of a large number density of ice crystals with a relatively low ice mass and an

effective diameter of approximately 5-10 µm while the edge of the contrail has a low number density but uptakes a large part of the surrounding water vapor, leading to a spatially non-uniform contrail ice mass.

Gravitational sedimentation causes larger crystals to fall more rapidly leading to a vertical layering of crystals with different sizes. Due to colder temperatures, ambient supersaturation on the upper side of the contrail enhances the ice crystal growth rate, and thus generates larger crystals.

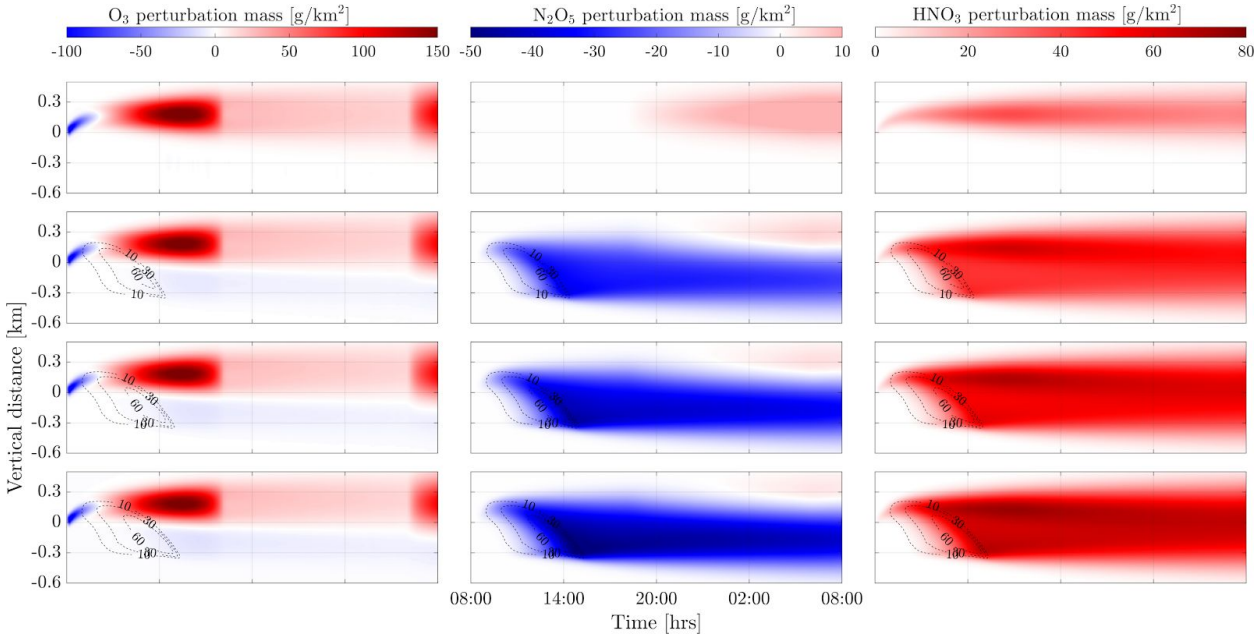

Figure S5: Contours of horizontally-integrated O_3 (left), N_2O_5 (center) and HNO_3 (right) plume perturbations for different black carbon emission scenarios: 0, 20, 40 and 60 mg/kg$_{fuel}$ (from top to bottom) in upper tropospheric conditions. Dashed lines show contours of the horizontal ice water path in g/m^2. A wind shear of 0.002 s^{-1} is applied.

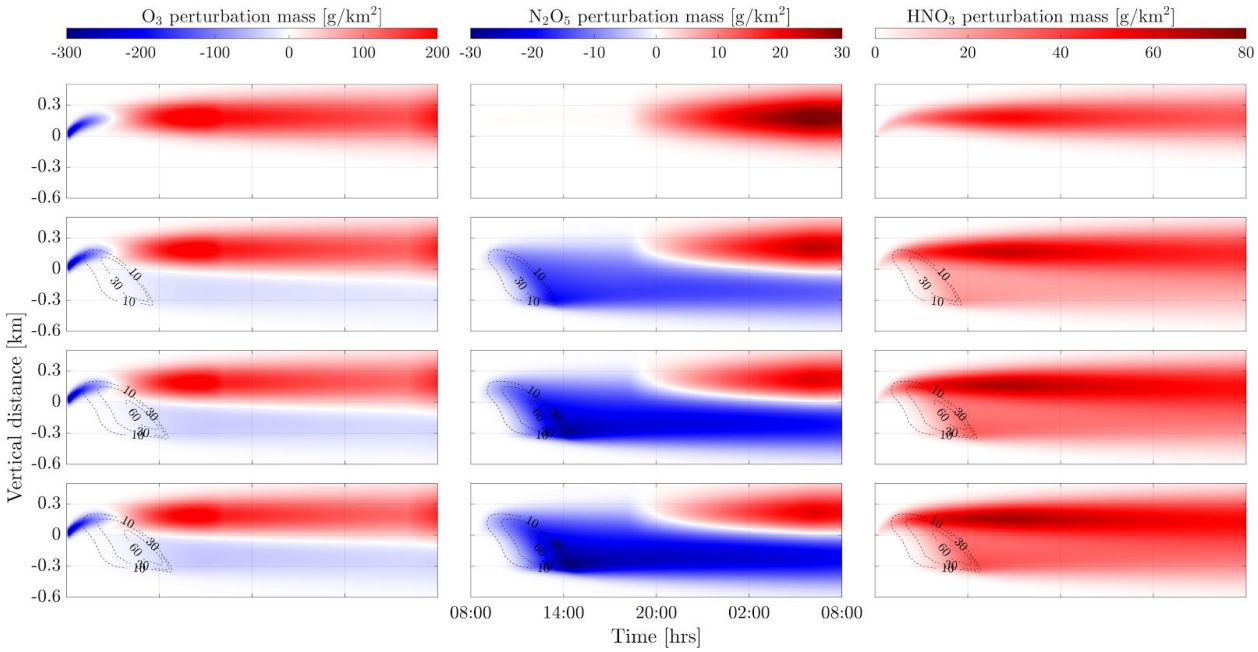

Figure S6: Contours of horizontally-integrated O_3 (left), N_2O_5 (center) and HNO_3 (right) plume perturbations for different black carbon emission scenarios: 0, 20, 40 and 60 mg/kg$_{fuel}$ (from top to bottom) under lower stratospheric conditions. A similar background relative humidity as Figure 5 was applied. Dashed lines show contours of the horizontal ice water path in g/m^2.

In addition to changing the optical properties of the contrail, the black carbon emissions index affects the chemical impact of the plume. Figure S5 and S6 show the evolution of several key chemical species over the contrail lifetime for upper tropospheric and lower stratospheric conditions respectively. Perturbations of O_3, N_2O_5, and HNO_3 are displayed for each scenario. The horizontal ice water path is also displayed, showing the location and extent of the contrail. Asymmetry in the vertical profiles arises because of gravitational settling of ice crystals and heterogeneous chemistry on their surface.

The stratospheric case displays stronger chemical production rates, but the relative differences from a change in the black carbon emission scenario are greater in tropospheric conditions.

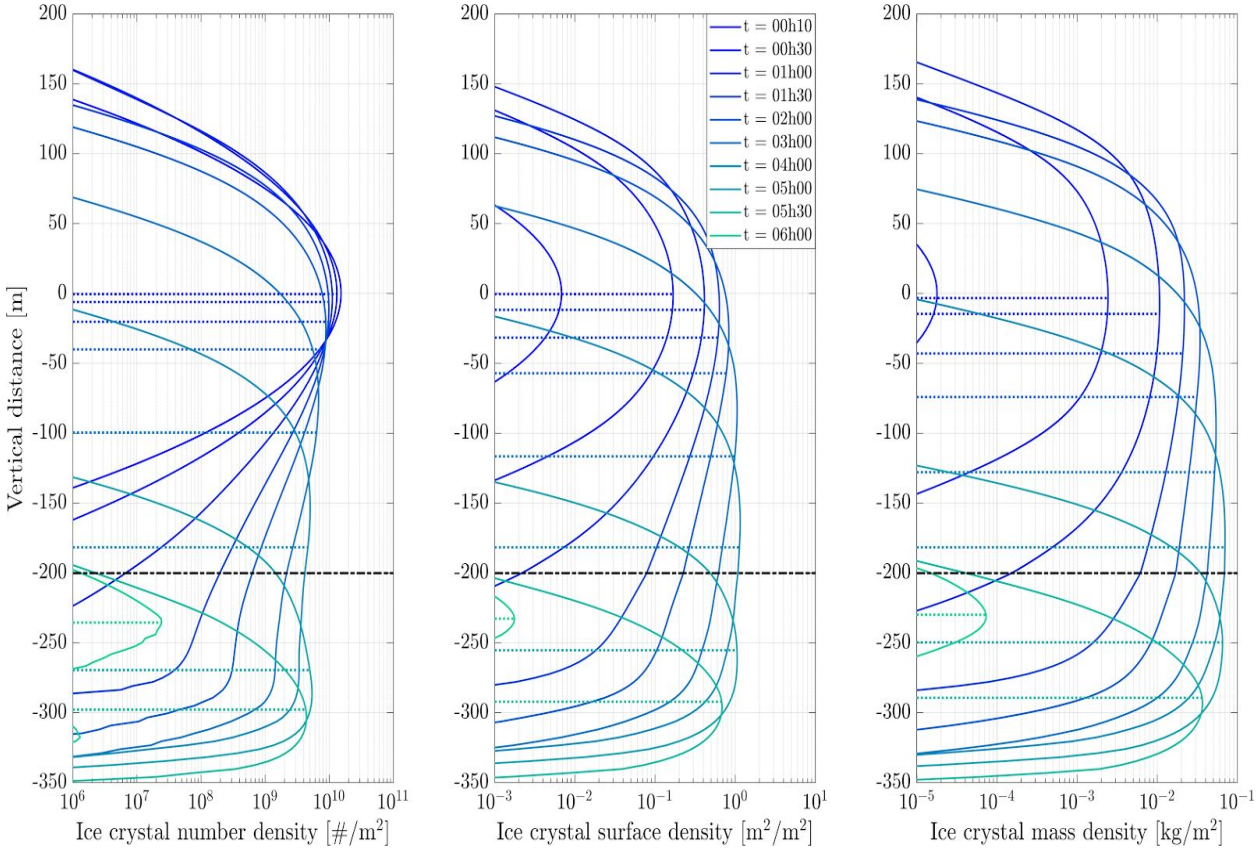

Figure S7: Time evolution of horizontally-integrated ice crystal number, surface and mass densities. The color gradient refers to the contrail age. The supersaturation region extends from ±200 m around the flight altitude (represented as a dash-dotted black line). The median of each distribution is plotted as a dotted line.